Origins of R_2^* orientation dependence in gray and white matter

David A. Rudko[a,b], **L. Martyn Klassen**[b], **Sonali N. de Chickera**[c], **Joseph S. Gati**[b], **Gregory A. Dekaban**[c,d], **and Ravi S. Menon**[a,b,1]

[a]Department of Physics and Astronomy, University of Western Ontario, London, ON, Canada N6A 3K7; [b]Center for Functional and Metabolic Mapping and [c]Molecular Brain Research Group, Robarts Research Institute, London, ON, Canada N6A 5B7; and [d]Department of Microbiology and Immunology, University of Western Ontario, London, ON, Canada N6A 5C1

Edited by Marcus E. Raichle, Washington University in St. Louis, St. Louis, MO, and approved November 27, 2013 (received for review April 5, 2013)

Estimates of the apparent transverse relaxation rate (R_2^*) can be used to quantify important properties of biological tissue. Surprisingly, the mechanism of R_2^* dependence on tissue orientation is not well understood. The primary goal of this paper was to characterize orientation dependence of R_2^* in gray and white matter and relate it to independent measurements of two other susceptibility based parameters: the local Larmor frequency shift (f_L) and quantitative volume magnetic susceptibility ($\Delta\chi$). Through this comparative analysis we calculated scaling relations quantifying R_2' (reversible contribution to the transverse relaxation rate from local field inhomogeneities) in a voxel given measurements of the local Larmor frequency shift. R_2' is a measure of both perturber geometry and density and is related to tissue microstructure. Additionally, two methods (the Generalized Lorentzian model and iterative dipole inversion) for calculating $\Delta\chi$ were compared in gray and white matter. The value of $\Delta\chi$ derived from fitting the Generalized Lorentzian model was then connected to the observed R_2^* orientation dependence using image-registered optical density measurements from histochemical staining. Our results demonstrate that the R_2^* and f_L of white and cortical gray matter are well described by a sinusoidal dependence on the orientation of the tissue and a linear dependence on the volume fraction of myelin in the tissue. In deep brain gray matter structures, where there is no obvious symmetry axis, R_2^* and f_L have no orientation dependence but retain a linear dependence on tissue iron concentration and hence $\Delta\chi$.

MRI contrast mechanisms | grey matter | cellular architecture | relaxation times

In many neurological diseases such as multiple sclerosis, Alzheimer's, and Parkinson, and in conditions following traumatic brain injury, microstructural changes occur in gray and white matter (1–4). One method for quantifying these microstructural changes is the mapping of the effective transverse relaxation rate (R_2^*). Along with the longitudinal relaxation rate (R_1) and transverse relaxation rate (R_2), R_2^* has been viewed as a fundamental MRI tissue parameter, affected by several factors including myelin content (5, 6), endogenous ferritin-based (Fe^{3+}) iron (7, 8), tissue microstructure (6), and paramagnetic, blood deoxyhemoglobin (9). However, a number of recent studies have reported a somewhat surprising dependence of R_2^* on tissue orientation, at least in white matter (10–12). The purpose of this paper was to investigate the mechanisms that could contribute to this orientation dependence of R_2^* in both gray and white matter. Because R_2^* is influenced by magnetic field perturbations, we examined the role of local Larmor frequency shift (f_L) and quantitative magnetic susceptibility ($\Delta\chi$), parameters that relate field and frequency. Through this analysis we identified unique scaling relations that relate R_2' to the local Larmor frequency shift calculated after removal of macroscopic field inhomogeneities. Additionally, we compared two methods for computing $\Delta\chi$ in gray and white matter: (*i*) fitting the Generalized Lorentzian (GL) model of field perturbers (13) to f_L measured at multiple brain orientations and (*ii*) magnitude-regularized dipole inversion (14). The difference between these two estimates represents the local frequency shift due to a cylindrical, axon geometry and is a marker of axonal integrity.

Having modeled the orientation dependence, we next examined the effect of myelin and iron on both R_2^* and $\Delta\chi$. We demonstrated a linear correlation between these quantities and optical density (OD) derived from diaminobenzidine (DAB)-enhanced Perls stain (sensitive to ferritin-based iron) for cortical gray matter. Similarly, using OD derived from solochrome cyanine-R (ScR)–stained slides in rat brain major white matter fiber regions, we showed strong positive correlations between the transverse relaxation constants, R_2 and R_2', and myelin density. Taken together, our results demonstrate that observed R_2^* values in ex vivo brains can be explained by a sinusoidal dependence on tissue microstructure orientation in conjunction with a linear dependence on the myelin concentration in cortical gray and white matter. In deeper gray matter structures with no preferred symmetry axis, R_2^* does not have an orientation dependence but retains a linear dependence on iron concentration.

Theory

Orientation Dependence of R_2^* in White Matter. Recently, Lee et al. (12) used a theoretical model developed by Yablonskiy and Haacke (15) to fit an orientation-dependence curve to R_2^* data from ex vivo, fixed human corpus callosum at 7 T. The model assumes that the orientation dependence of R_2^* in groups of close-packed, parallel white matter fibers can be approximated with the following equation:

Significance

Differences in the apparent transverse relaxation rate (R_2^*) between tissues are exploited in numerous magnetic resonance imaging (MRI) techniques from functional MRI to susceptibility weighted imaging. Recent results show a surprising dependence of tissue R_2^* on orientation. This study demonstrates that the orientation dependence of R_2^* in both white and cortical gray matter has a sinusoidal dependence on tissue orientation and a linear dependence on the perturber volume fraction (measured by quantitative histology). A biophysical model is used to relate the observed orientation dependence to the local Larmor frequency shift and volume magnetic susceptibility of the tissue.

Author contributions: D.A.R. and R.S.M. designed research; D.A.R., L.M.K., S.N.d.C., J.S.G., and G.A.D. performed research; G.A.D. contributed new reagents/analytic tools; D.A.R. and R.S.M. analyzed data; and D.A.R. and R.S.M. wrote the paper.

The authors declare no conflict of interest.

This article is a PNAS Direct Submission.

[1]To whom correspondence should be addressed. E-mail: rmenon@robarts.ca.

This article contains supporting information online at www.pnas.org/lookup/suppl/doi:10.1073/pnas.1306516111/-/DCSupplemental.

$$R_2^*(\theta) = C_0 + C_1 \sin(2\theta + \psi_0), \quad [1]$$

where C_0, C_1, and ψ_0 are constants and θ is the angle of the longitudinal axis of the fiber tract relative to the B_0 field. Eq. **1** is an extension of the standard relationship for R_2^*:

$$R_2^* = R_2 + R_2'. \quad [2]$$

The C_0 constant in Eq. **1** represents the conventional transverse relaxation rate, R_2, as well as any contributions to R_2' that are not angularly dependent (e.g., R_2' shifts due to endogenous ferritin-based iron). For white matter fiber bundles, the constant C_1 is defined as

$$C_1 = 2\pi \ \omega_0 \ \zeta \ \Delta\chi, \quad [3]$$

where the variable ζ represents the volume fraction of field perturbers and $\Delta\chi$ represents the magnetic susceptibility difference between a fiber bundle and the medium surrounding the bundle. In this paper, we validated the orientation-dependence model of Eq. **1** (specifically, the relation $C_1 = 2\pi \ \omega_0 \ \zeta \ \Delta\chi$) by comparing the fitted parameters from the linear R_2^* model to the value of $\Delta\chi$ calculated from the GL model of field perturbers (further discussed in *Orientation Dependence of f_L in White Matter*). To perform this comparison, the OD of myelin obtained from histochemical staining and slide registration was used as a surrogate for the volume fraction (ζ). Throughout this paper we define the R_2' value as being the same as C_1. According to the original derivation (15), the true value of R_2' for a network of parallel fibers is $2\pi \ \omega_0 \ \zeta \ \Delta\chi \ \sin(2\theta)$. Because we are explicitly modeling the orientation dependence of R_2', we use the constant C_1 to define the amplitude of the R_2' variation with fiber angle. Consequently, we treat C_1 as a surrogate measure of R_2'.

The orientation dependence of the R_2^* signal has also been characterized with an alternative, second-order model of field perturbers. This model postulates that two distinct components contribute to the orientation dependence of R_2^* in white matter: (*i*) an isotropic component associated with the cylindrical geometry of myelinated axons (13) and (*ii*) an anisotropic component associated with the phospholipid bilayer structure of myelin (12). The equation for the second-order model is

$$R_2^*(\theta) = C_0 + C_1 \sin(2\theta + \psi_0) + C_2 \sin\left(4\theta + 2\psi_0 - \frac{\pi}{2}\right). \quad [4]$$

In this study, we compared the linear and second-order R_2^* models in rat brain major white matter fiber bundles.

Orientation Dependence of R_2^* in Gray Matter. Eq. **1** was also used to fit R_2^* orientation dependence in gray matter. The orientation of gray matter was defined as the angle between the normal to the cortical surface and B_0. This technique, previously used by Cohen-Adad et al. (16), is physically motivated by the fact that myelinated white matter tracts project into cortical gray matter where they synapse onto cortical neurons, conferring a preferred axis of symmetry in the cortical gray matter.

Orientation Dependence of f_L in White Matter. The theoretical field shift around a susceptibility inclusion has conventionally been calculated in NMR using the Lorentzian sphere formalism. However, this approach has been questioned for modeling brain tissue structures such as axons that have nonspherical boundaries. Instead, an alternative GL model has been suggested by He and Yablonskiy (13) for modeling field perturbers in the static dephasing regime. This model, with application to external capsule white matter in rat brain, is discussed in detail in what follows.

The external capsule is a large white matter tract that extends longitudinally through the rat brain in the anterior–posterior direction. The local Larmor frequency shift of water molecules moving inside parallel axons of the external capsule bundle relative to the external gray matter can be calculated using the Lorentzian cylinder approximation of He and Yablonskiy (13). In this approximation, a model Lorentzian cylinder surrounds the white matter bundle and has a diameter larger than that of the bundle. The nuclei of water molecules inside the axon bundle experience a frequency shift that is the summation of the contributions from point magnetic dipoles which exist either (*i*) inside or (*ii*) outside a Lorentzian cylinder. The magnetic field experienced by nuclei due to dipoles existing inside the Lorentzian cylinder averages to 0 because the average magnetic field around a point dipole is 0. Consequently, the frequency shifts of the nuclei inside the external capsule are influenced by point dipoles in the medium outside the cylinder of Lorentz.

Along the anterior–posterior direction, the external capsule bundle can be considered as an infinite circular cylinder with a length significantly larger than its diameter. In this regime, we can write the frequency shift for external capsule white matter as

$$\frac{f_{L,WM}}{f_0} = -2\pi(\chi_{ae} - \chi_{WM}) \cdot \left(\cos^2\theta - \frac{1}{3}\right), \quad [5]$$

where $f_{L,WM}$ is the local frequency shift in the white matter relative to the surrounding, isotropic gray matter medium, χ_{ae} (ppm) is the magnetic susceptibility of the isotropic medium surrounding the axon bundle, $\chi_{WM} = 0.067$ ppm is the magnetic susceptibility of myelin in white matter (13), and θ is the orientation angle of an axon bundle relative to the B_0 field.

Throughout this paper, $\Delta\chi$, calculated by fitting the GL model (Eq. **5**) to f_L measured with varying brain orientations, is denoted as $\Delta\chi_{GLModel}$ to differentiate it from the magnetic susceptibility calculated using a regularized dipole inversion method ($\Delta\chi_{dipole}$) outlined further below. All magnetic susceptibility values are written in SI units and are calculated relative to the average magnetic susceptibility in an adjacent cortical gray matter region of interest (ROI).

Orientation Dependence of f_L in Gray Matter. We also examined the orientation dependence of f_L in cortical gray matter. The presence of cortical fibers should, theoretically, gives rise to an orientation dependence described by Eq. **5**. We tested this hypothesis in cortical gray matter regions evenly distributed around the cortex. The $\Delta\chi = \chi_{ae} - \chi_{WM}$ term in Eq. **5** was replaced by $\Delta\chi = \chi_{ae} - \chi_{GM\_average}$ where $\chi_{GM\_average}$ is the average susceptibility of gray matter measured from multiple ROIs evenly distributed around the cortex.

Reconstruction of Quantitative Susceptibility Maps from Single-Orientation f_L Maps. According to Maxwell's equations, a volume magnetic susceptibility distribution, $\Delta\chi$ [parts per billion (ppb)], produces an associated local frequency shift, f_L (Hz). Defining the k-space representation of f_L as $f_L(k)$ and the k-space representation of $\Delta\chi$ as $\Delta\chi\ (k)$, the local resonance frequency map is related to the volume magnetic susceptibility as follows (14, 17, 18):

$$f_L(k) = \left(\frac{1}{3} - \frac{k_z}{k^2}\right) \cdot \Delta\chi\ \ (k). \quad [6]$$

Calculation of $\Delta\chi_{dipole}$ maps from the f_L requires inversion of Eq. **6**. A common method used for this inversion is quadratic minimization of a regularized, least-squares objective function (14). The technique from ref. 14 was used for calculation of $\Delta\chi_{dipole}$ in this work by implementing a regularized conjugate gradient normal residual (CGNR) algorithm in MATLAB (R2008b, MathWorks).

Calculation of magnetic susceptibility in this study was performed using a single orientation.

Results and Discussion

Imaging Setup. Each of three rat brain samples was imaged using a multiecho gradient-echo sequence with the medial fissure of the brain oriented at 18 different sampling angles relative to the main field of the magnet. Specifically, the brains were rotated to (*i*) 8 unique angles of $n \times 45°$ ($n = 1\ldots8$) around the *y* axis shown in Fig. 1*C*, as well as (*ii*) 10 additional angles chosen to produce an even sampling of the unit sphere. Reproducible rotations were achieved by using the sample holder shown in Fig. 1.

Orientation Dependence of R_2^* in White Matter. Fig. 2*B* illustrates the change in R_2^* as a function of the orientation of the four ROIs in the external capsule. Statistically significant changes in the white matter R_2^* for different brain orientations were observed at the confidence level of $P < 0.01$. This significance level was computed using a balanced one-way ANOVA for comparing independent samples containing mutually independent observations. The orientation dependence of R_2^* was well fit by a $\sin(2\theta + \psi_0)$ relationship, with an average peak-to-peak variation of $\Delta R_2^* = 3.11 \pm 0.62\ \mathrm{s}^{-1}$ (averaged across all external capsule ROIs in both hemispheres).

The linear and second-order R_2^* models of Eqs. **1** and **4** were both fit to the R_2^* data in white matter. From fitting of the linear model, three parameters, C_1, C_0, and ψ_0, related to tissue composition (12) were then calculated. The full set of derived parameters for all rat brains are listed in Table 1. To generate those values, the linear model was fit to the data in each ROI of Fig. 2*A* for each brain sample. The fitted values for external capsule ROIs in the same hemisphere for the same sample were then averaged. A C_0 value of $62.13 \pm 0.54\ \mathrm{s}^{-1}$ was observed when all external capsule white matter ROIs were averaged ($n = 3$). A two-tailed Welch's *t* test revealed no statistically significant difference ($P < 0.05$) between C_0 computed in the left- and right-brain external capsule.

The second-order model (Eq. **4**) was also fit to the R_2^* orientation data in external capsule white matter. The derived parameters are listed in Table S1. The correlation coefficients in Table S1 demonstrate that the second-order model did not provide significantly improved fitting. For this reason no further analysis was conducted with this higher-order model. Application of the higher-order model is difficult due to the confounding contributions of residual background fields [which may also have a $\sin(4\theta)$ dependence]. In previous studies, signal-to-noise ratio (SNR) considerations revealed that large ROIs are necessary for observing the $\sin(4\theta)$ component. Such large ROIs are prone to introducing error in the measured R_2^* orientation dependence because the mean value of R_2^* calculated from a large ROI is more sensitive to background fields. Such fields may vary over the length scale of the ROIs (12). Moreover, ROI-based analysis precludes voxel-wise interpretation of the anisotropic component, which is the ultimate goal of fitting the proposed second-order model.

Orientation Dependence of R_2^* in Gray Matter. Fig. 2*F* displays the changes in R_2^* of cortical gray matter as the brain was rotated. Gray matter R_2^* varied sinusoidally with surface normal orientation and was well fit by the linear model. The average trough-to-peak R_2^* variation in the cortex was $\Delta R_2^* = 0.94 \pm 0.32\ \mathrm{s}^{-1}$ (averaged across all gray matter ROIs in both hemispheres). The parameters derived from fitting the linear model in gray matter are listed in Table 2. The parameter C_1 was used to estimate the trough-to-peak change in R_2^*.

R_2^* of subcortical gray matter did not display significant changes with brain orientation (Fig. 2 *I* and *J*). The ROIs for this analysis were chosen in the subcortical, lateral habenular nucleus. The notable difference between Fig. 2*F* (cortical gray matter) and Fig. 2*J* (deep gray matter) supports the premise that the orientation of penetrating cortical white matter fibers affects estimates of monoexponential R_2^* in gray matter. Further, it identifies that changes in R_2^* with brain orientation in the largely isotropic structures (e.g., glial cells and astrocytes) of the basal ganglia are insignificant. It is not possible to completely exclude the contribution of coherently oriented microvasculature structures from the orientation-dependent R_2^* in cortical gray matter. Further work is necessary to completely evaluate the quantitative contribution of cortical microvasculature to the orientation-dependent R_2^* signal.

Orientation Dependence of f_L in White Matter. The relationship between f_L and white matter fiber orientation is illustrated in Fig. 2*C*. The mean trough-to-peak amplitude of the f_L shift was 7.2 ± 3.8 Hz. Fibers oriented perpendicular to the B_0 field had a positive frequency shift compared with those oriented parallel to the field. This trend is characteristic of any substance that is less diamagnetic than water. For instance, when myelin becomes less diamagnetic than water due to the fixation process (19, 20), this trend is observed. The results are consistent with previously observed effects of fixation on the magnetic susceptibility of myelin (22). The average $\Delta\chi_{GLModel}$ measured in external capsule white matter was 24.9 ± 2.25 ppb. This compares very well to previous values of 26 ppb in mouse white matter (6).

Fig. 2*D* identifies a linear relationship between the orientation dependencies of R_2^* and f_L in the oriented white matter fibers of the external capsule. The specific linear relation is given by $R_2^* = 0.23 \cdot f_L + 65.28$. The influence of R_2 is represented by the vertical offset term ($65.28\ \mathrm{s}^{-1}$), whereas a scaling constant which relates R_2' to f_L is given by the slope of the line (0.23). R_2' is influenced by the local frequency shift in a voxel for each tissue geometry and tissue composition (15). Breaking down the respective contributions of R_2 and R_2' in this manner may be useful in identifying subtle changes occurring in gray and white matter in the course of disease development. For instance, demyelination in multiple sclerosis may preferentially affect R_2' while leaving R_2 unchanged.

Orientation Dependence of f_L in Gray Matter. The relationship between cortical gray matter f_L and cortical fiber orientation is illustrated in Fig. 2*G*. The data were well fit by the GL model of Eq. **3**. The average amplitude of gray matter f_L variation was

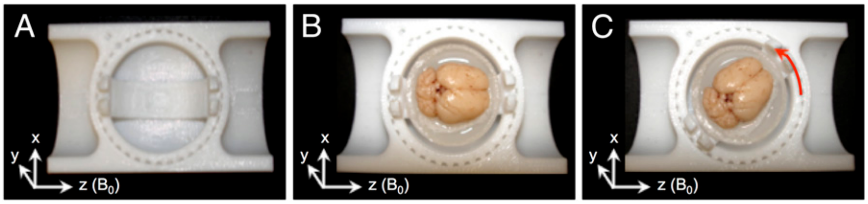

Fig. 1. (*A*) Custom-machined sample container and (*B* and *C*) experimental setup illustrating rat brain immersed in MRI invisible, fluorinated fluid. Each increment on the sample container represents a 10° rotation around the *y* axis.

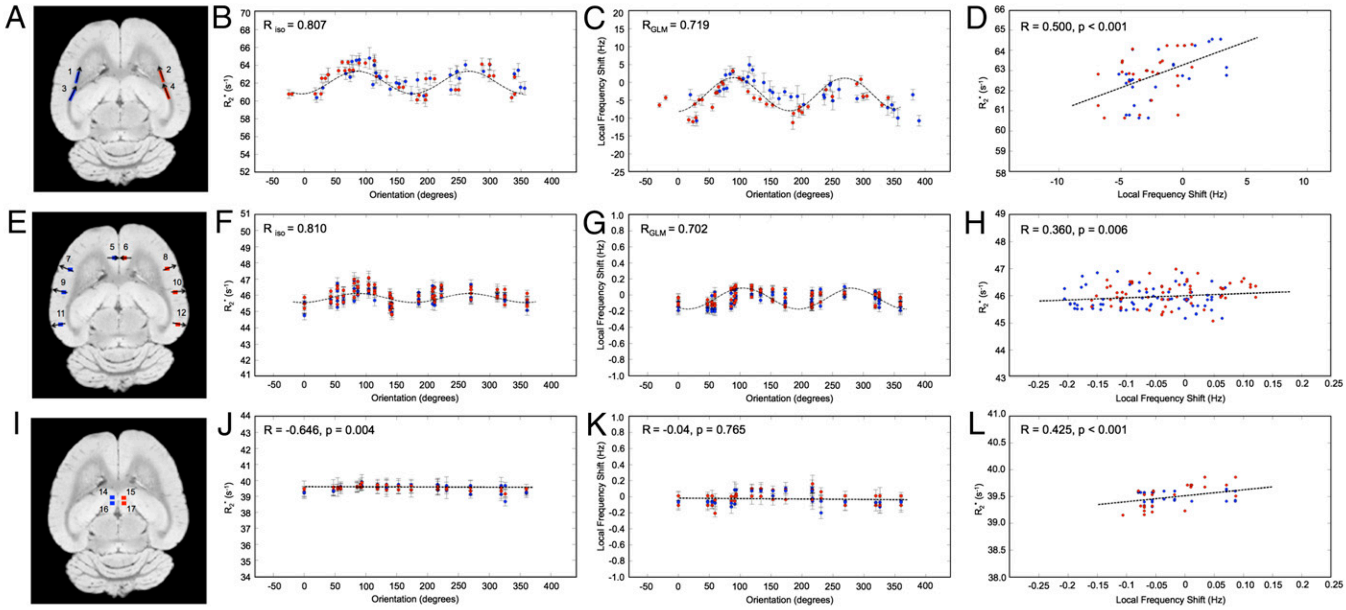

Fig. 2. R_2^* and f_L changes observed in gray and white matter as a function of fiber orientation relative to B_0 (for white matter) and surface normal orientation relative to B_0 (for gray matter). The ROIs used for this analysis are displayed in *A*, *E*, and *I*. The linear R_2^* model is overlaid on *B* and *F*. The GL model fit is overlaid on *C* and *G*. *J* and *K* demonstrate the R_2^* and f_L changes observed in the basal ganglia structures as a function of brain orientation. *D*, *H*, and *L* demonstrate the linear relationships between the orientation dependence of R_2^* and f_L in white and gray matter. Error bars in *B*–*D*, *F*–*H*, and *J*–*L* represent SEM.

0.56 ± 0.13 Hz. Table 3 (right-most columns) shows the values of $\Delta\chi$ calculated from the GL model fit. The average $\Delta\chi_{GLModel}$ measured in gray matter was 4.5 ± 1.39 ppb. Currently, there are no examples in the literature of values for magnetic susceptibility in gray matter obtained from the GL model with which to compare this result. However, the $\Delta\chi_{GLModel}$ can be compared with $\Delta\chi_{dipole}$, as performed in *Comparison of* $\Delta\chi_{GLModel}$ *with* $\Delta\chi_{dipole}$ *in White Matter*. The ROIs used for this analysis of f_L orientation dependence in cortical gray matter were chosen with reference to an adjacent intracortical vein but not including this vein. The ROIs were specifically selected using f_L maps to avoid including local fields from large intracortical veins which can modulate f_L (21).

The influence of capillary veins can also modulate an orientation-dependent f_L contrast in cortical gray matter (9). In ref. 9 the influence of capillary deoxyhemoglobin on f_L in rat brain in vivo was carefully measured and found to be negligible relative to the bulk gray/white f_L contrast (maximum $\Delta f_L = 0.02$ Hz for realistic values of oxygen saturation, $Y = 0.7$, and hematocrit, $\mathrm{Hct} = 0.4$, in rat brain capillary). Close examination of our myelin-stained slides (e.g., see Fig. 5*A*) in the cortical ROIs revealed the presence of striated myelin variation across the length of the cortex but no clear evidence of larger capillary veins. For these reasons, we believe that capillary-mediated f_L shifts negligibly contributed to the cortical gray matter orientation-dependent f_L variations observed in this study.

The orientation dependence of f_L was also evaluated in subcortical gray matter. Four ROIs were chosen in the left- and right-brain lateral habenular nuclei (Fig. 2*I*). No distinct orientation dependence for f_L (Fig. 2*K*) was observed. This result is similar to the orientation dependence of R_2^* in subcortical gray matter and distinct from f_L of cortical gray matter which does show a subtle orientation dependence (Fig. 2*G*). This indicates the local frequency shift is sensitive to cellular architectural differences in different gray matter regions.

Fig. 2 *H* and *L* identifies linear relationships between the orientation dependencies of R_2^* and f_L for cortical and subcortical gray matter. For cortical gray matter, $R_2^* = 0.82 \cdot f_L + 49.27$, whereas for subcortical gray matter, $R_2^* = 1.10 \cdot f_L + 39.51$. These linear relations identify the contribution of the local frequency shift to R_2^* through the R_2' value. Two scaling relations were found: $R_2' = 0.82 \cdot f_L$ for cortical gray matter and $R_2' = 1.10 \cdot f_L$ for subcortical gray matter. The scaling constant relating R_2' to f_L in cortical gray matter (0.82) was 3.57 times larger than that of white matter (0.23). However, the mean amplitude of the f_L variation in white matter is ~20 times larger than that of cortical gray matter ($\Delta f_L = 4$ Hz for white matter compared with $\Delta f_L = 0.2$ Hz for gray matter). Together, these factors indicate that the

Table 1. Parameters derived from fitting the linear R_2^* model in external capsule white matter

ROI location	C_0, s^{-1}	C_1, s^{-1}	ψ_0, °	*r*
Left brain, S1	59.89 ± 0.27	2.47 ± 0.37	11.74 ± 9.28	0.849
Right brain, S1	59.36 ± 0.16	1.05 ± 0.23	32.58 ± 11.93	0.750
Left brain, S2	64.23 ± 0.11	1.53 ± 0.11	22.84 ± 5.23	0.926
Right brain, S2	64.71 ± 0.23	1.83 ± 0.32	21.73 ± 10.36	0.833
Left brain, S3	62.14 ± 0.26	1.23 ± 0.39	15.23 ± 16.82	0.633
Right brain, S3	62.47 ± 0.24	1.21 ± 0.32	21.39 ± 16.53	0.702

Data are shown for each of the three brain samples (e.g., S1 = brain sample 1). Pearson correlation coefficients (*r*) are given in the right-most column of the table.

Table 2. Results of the linear model fit to R_2^* in gray matter

ROI location	C_0, s^{-1}	C_1, s^{-1}	ψ_0, °	*r*
Left brain, S1	46.36 ± 0.16	0.41 ± 0.16	18.02 ± 7.89	0.718
Right brain, S1	45.10 ± 0.08	0.56 ± 0.07	20.50 ± 4.09	0.810
Left brain, S2	46.88 ± 0.18	0.62 ± 0.15	13.52 ± 10.06	0.659
Right brain, S2	47.11 ± 0.22	0.42 ± 0.27	24.19 ± 23.98	0.514
Left brain, S3	46.68 ± 0.11	0.34 ± 0.10	31.85 ± 9.07	0.745
Right brain, S3	46.57 ± 0.12	0.38 ± 0.09	43.16 ± 6.27	0.796

Data are shown for each of the three brain samples (e.g., S1 = brain sample 1). Pearson correlation coefficients (*r*) are given in the right-most column of the table.

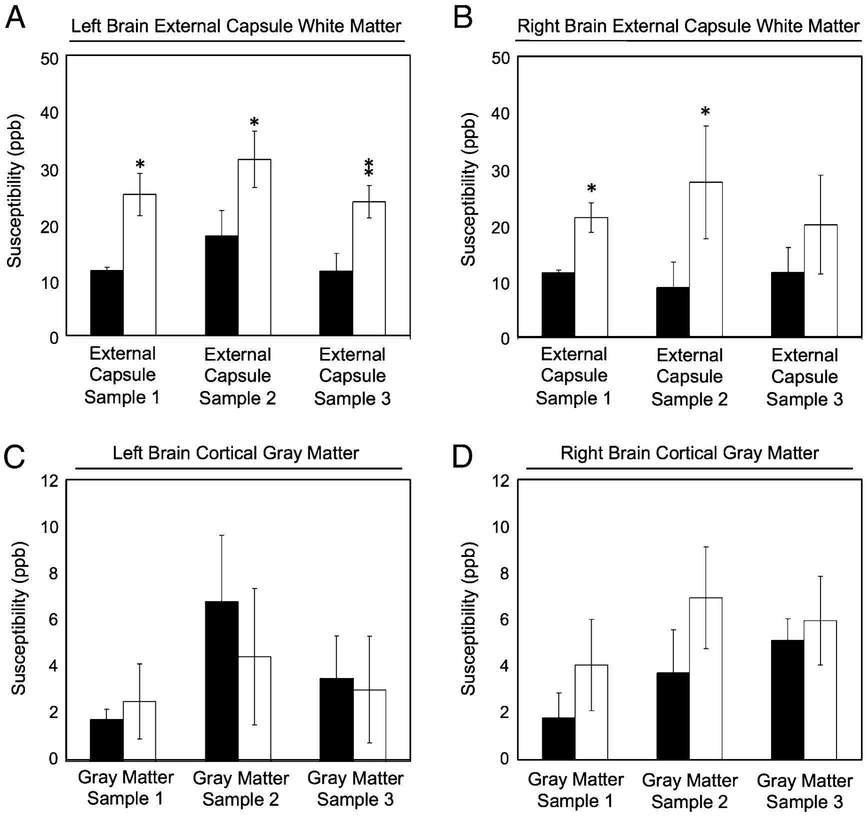

Fig. 3. Comparison of $\Delta\chi_{dipole}$ (black bars) with $\Delta\chi_{GLModel}$ (white bars) for both white matter (*A* and *B*) and gray matter (*C* and *D*). All susceptibility values are in SI units of ppb and have been referenced to the susceptibility of gray matter in an adjacent ROI. Separate comparisons were performed for left- and right-brain hemispheres. Error bars represent SEM. Statistical significance levels are defined as: $^*P < 0.05$ and $^{**}P < 0.001$.

orientation-dependent, reversible component of the transverse relaxation rate (R_2'= constant·f_L) is ~5.60 times larger in white matter compared with gray matter (for the case of this fixed rat brain tissue). This R_2' difference is a function of the tissue microstructure because it is a function of both axonal density and fiber orientation dispersion inside a voxel (15).

The measurement of local frequency shift through unwrapping the phase, then, serves as an approximate alternative for measuring R_2' in gray matter. This may be useful for probing changes in microstructure of gray matter associated with disease.

Comparison of $\Delta\chi_{GLModel}$ with $\Delta\chi_{dipole}$ in White Matter. The histograms in Fig. 3 *A* and *B* compare $\Delta\chi_{GLModel}$ with $\Delta\chi_{dipole}$ for each sample in each hemisphere. Table 3 shows the white matter susceptibility values calculated from fitting the GL model and associated Pearson correlation values. A Welch's two-tailed *t* test revealed that the GL model-derived and the inversion-calculated values of magnetic susceptibility in the external capsule were different ($P < 0.05$) in all cases except for the right hemisphere of sample 3, where the mean value of $\Delta\chi_{GLModel}$ is still larger than that of $\Delta\chi_{dipole}$. The difference between these two measurements was on average 12.73 ± 2.91 ppb. This difference results from the fact that the GL model accounts for the geometry-induced frequency shift of cylindrical axons, whereas dipole fitting does not.

The magnitude of the isotropic component of the frequency shift in white matter is affected by formalin fixation. Recent research (22) conducted using excised rat brain optic nerve embedded in water suggests that the amplitude of this isotropic frequency shift is increased (this is a diamagnetic shift) by a factor of approximately 2, due to fixation. For this reason, the isotropic frequency shifts reported in our paper may be larger than those observed in fresh rat brain tissue.

The GL model does not account for susceptibility variations in white matter due to either chemical exchange or myelin bilayer anisotropy. Nevertheless, it is a useful model that can improve estimates of susceptibility, provided the fiber angle relative to B_0 is known. Interestingly, the difference of 12.73 ± 2.91 ppb between $\Delta\chi_{GLModel}$ and $\Delta\chi_{dipole}$ is on the order of the isotropic magnetic susceptibility of white matter recently calculated in mouse brain using susceptibility tensor imaging (13 ppb reported in ref. 6). These convergent results suggest that fitting the GL model to f_L measured at multiple brain orientations is a robust technique for quantifying the isotropic, geometry-derived component of susceptibility in white matter.

Table 3. Parameters calculated from the GL model fit of f_L vs. cortical surface normal orientation (for gray matter) and f_L vs. principal fiber orientation (for white matter)

	Gray matter		White matter	
ROI location	$\Delta\chi$, ppb	*r*	$\Delta\chi$, ppb	*r*
Left brain, S1	2.55 ± 1.60	0.871	25.13 ± 3.77	0.780
Right brain, S1	4.04 ± 1.96	0.734	20.11 ± 2.64	0.759
Left brain, S2	4.46 ± 2.91	0.736	31.40 ± 5.03	0.654
Right brain, S2	6.92 ± 2.18	0.940	27.60 ± 7.03	0.783
Left brain, S3	3.05 ± 2.28	0.670	23.88 ± 2.89	0.895
Right brain, S3	5.94 ± 1.89	0.840	21.36 ± 8.80	0.601

The susceptibility values are referenced to the average susceptibility of surrounding gray matter. Data are shown for each of the three brain samples (e.g., S1 = brain sample 1). Pearson correlation coefficients (*r*) are given in the right-most column of the table.

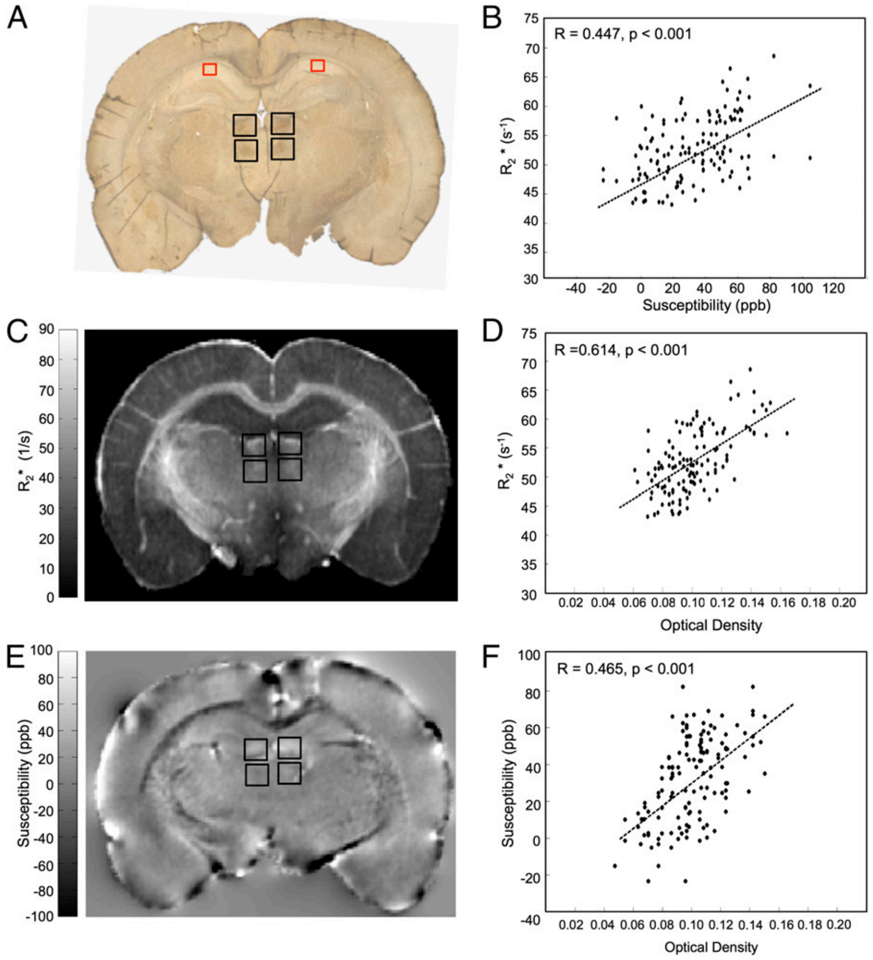

Fig. 4. R_2^* and quantitative susceptibility values in the lateral habenular and mediodorsal nuclei (deep brain basal ganglia structures) of the rat brain positively correlate with Fe^{3+} density from DAB-enhanced Perls staining. (*A*) A representative coronal section of a rat brain stained with DAB-enhanced Perls is shown. Black boxes indicate the ROIs in which OD and quantitative MRI values were measured (these same ROIs are also overlaid on both the R_2^* map in *C* and the QS map in *E*). ROIs include the right and left lateral habenular nuclei and the right and left mediodorsal nuclei. Red boxes indicate reference ROIs used in computation of OD. The corresponding coronal MRI sections of a rat brain are displayed in *C* for R_2^* (in units of 1/s) and *E* for quantitative susceptibility (in units of ppb). *B* displays a positive linear correlation between R_2^* and $\Delta\chi_{dipole}$ in the rat basal ganglia. The correlation of R_2^* (*D*) or $\Delta\chi_{dipole}$ (*F*) with OD measurements are also shown. Each data point represents a voxel from the chosen ROIs. The black dotted lines indicate the linear regression fit to the data. *R* and *P* values are indicated in the upper left-hand corner of the correlation plots.

Comparison of $\Delta\chi_{GLModel}$ with $\Delta\chi_{dipole}$ in Gray Matter. The histograms in Fig. 3 *C* and *D* compare $\Delta\chi_{GLModel}$ with $\Delta\chi_{dipole}$ for gray matter in each rat brain hemisphere. The values computed for $\Delta\chi_{GLModel}$ and the associated Pearson correlation coefficients are listed in Table 3. A Welch's two-tailed *t* test showed that $\Delta\chi_{GLModel}$ and $\Delta\chi_{dipole}$ are the same in all ROIs ($P > 0.05$ in all cases). This is not unexpected, given the observed variation in f_L with cortical fiber orientation in this study is very subtle (average amplitude of 0.56 ± 0.13 Hz for all ROIs examined).

From the above result, it can be inferred that, when gray matter susceptibility information is reconstructed using dipole inversion at standard clinical field strengths and at resolutions of 1 mm^3 isotropic, it is unlikely the effects of cortical fiber geometry on $\Delta\chi$ will be significant. However, this may not always be true for small animal studies. As susceptibility mapping methods improve and the achievable spatial resolution increases, the $\Delta\chi_{GLModel}$ value could serve as a standard for measurements of $\Delta\chi_{dipole}$ in cortical gray matter. Such a target value would facilitate analysis of convergence in regularized dipole inversion methods of quantitative susceptibility mapping.

Correlative Histology of MRI and Nonheme Iron in Rat Brain Basal Ganglia. Histological staining was performed to investigate the relationship between iron concentrations in rat brain tissue and susceptibility contrast parameters (R_2^* and $\Delta\chi_{dipole}$). Currently, there is significant interest in using a combination of R_2^* and $\Delta\chi_{dipole}$ to assess nonheme iron variations in human brain tissue (7, 23, 24). However, to date most studies have performed correlations between MRI susceptibility parameters in vivo and ex vivo iron concentrations derived from the literature (7). The quantitative relationship between iron concentration, as derived from OD of iron-stained slides, and both R_2^* and $\Delta\chi_{dipole}$ in the same tissue structure has not been examined.

To isolate the influence of iron on R_2^* and $\Delta\chi_{dipole}$, ROIs were chosen in rat basal ganglia regions containing high iron concentration and low myelin content. The ROIs were centered on the left lateral habenular and mediodorsal nuclei (black boxes in Fig. 4*A*). A positive correlation ($R = 0.614$, $P < 0.001$, Fig. 4*D*) between R_2^* and iron OD was observed according to the linear relation $R_2^* = 158.05 \cdot OD + 36.72$. This relation is specific to the field strength used in this study (9.4 T) due to the dependence of R_2^* on field strength. A similar positive correlation was found between $\Delta\chi_{dipole}$ and iron OD ($R = 0.465$, $P < 0.001$, Fig. 4*F*) with the linear regression fit: $\Delta\chi_{dipole} = 674.05 \cdot OD - 79.3$. R_2^*

was also plotted against corresponding $\Delta\chi_{dipole}$ on a voxel-by-voxel basis (Fig. 4*B*) to derive a relationship between these parameters for Fe^{3+} iron at 9.4 T. The linear relation between R_2^* and $\Delta\chi_{dipole}$ was $R_2^* = 0.10 \cdot \Delta\chi_{dipole} + 49.59$, with $R = 0.447$ and $P < 0.001$.

We observed a linear correlation between R_2^* and $\Delta\chi_{dipole}$ in the rat basal ganglia (Fig. 4*B*). In general, these two parameters need not be correlated (25); thus, this observation sheds some light on the underlying mechanisms governing these two quantities. Intervoxel susceptibility differences can result in a positive or negative frequency shift between voxels without contributing to the R_2^* of these voxels, whereas increased intravoxel susceptibility variation can lead to incoherent dephasing and increased R_2^* in a voxel. For the case of the basal ganglia, our data suggests that punctate nonheme iron concentrations in the brain are accompanied by magnetic field inhomogeneities on the scale of the voxel, thus affecting both R_2^* and $\Delta\chi_{dipole}$.

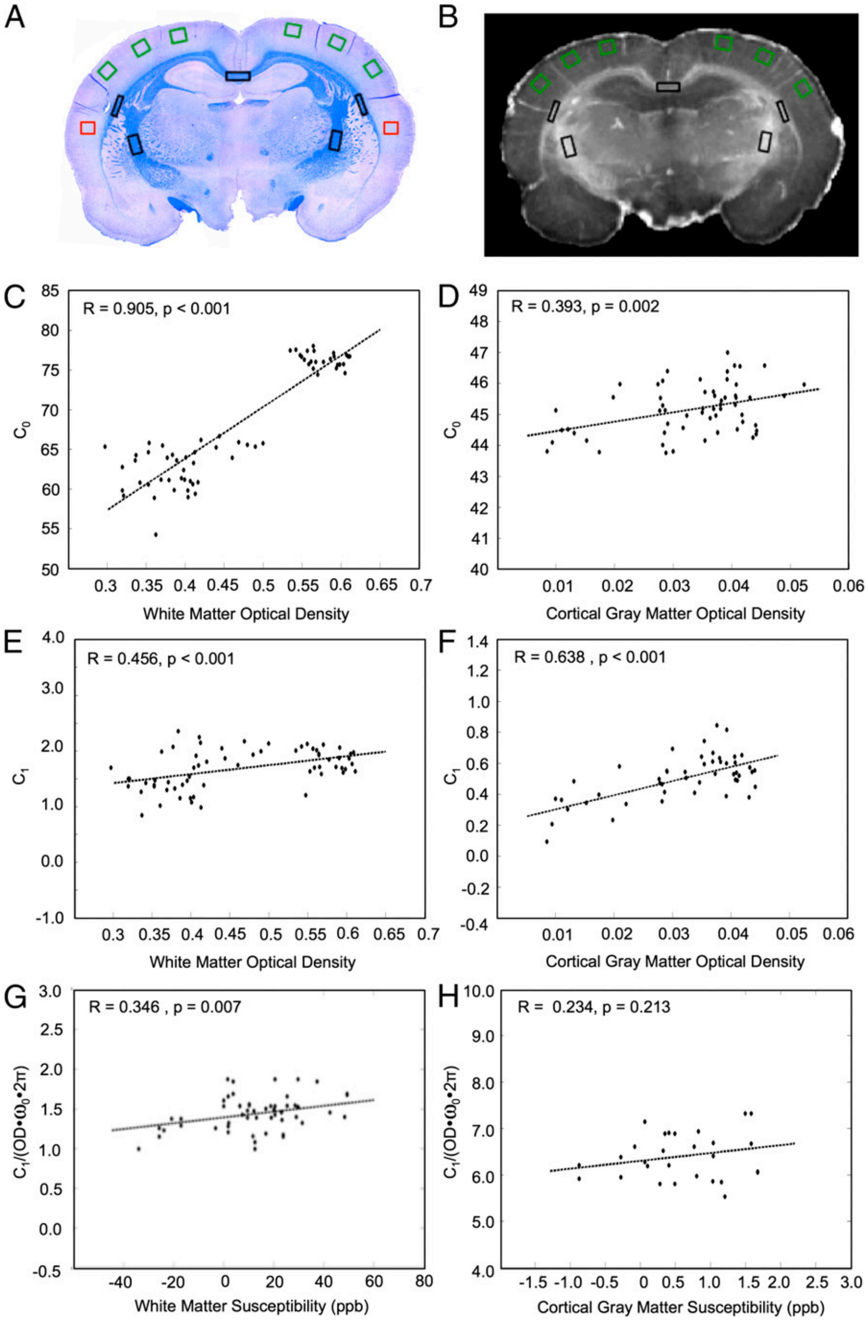

Fig. 5. The constants, C_0 and C_1, derived from the linear R_2^* orientation model correlate positively with OD of ScR staining for myelin in both major white matter tracts and cortical gray matter. (*A*) A representative coronal section of the rat brain stained for myelin. (*B*) R_2^* map corresponding to the myelin stain. Black boxes in *A* and *B* indicate the ROIs in which the OD of myelin, C_0 and C_1 were measured in white matter. Green boxes in *A* and *B* indicate the ROIs in which the OD of myelin, C_0 and C_1 were measured in cortical gray matter. Red boxes indicate reference ROIs employed in the computation of OD. C_0 (*C* and *D*) and C_1 (*E* and *F*) correlated positively with the myelin OD in major white matter tracts and cortical gray matter. Each data point represents a voxel from the chosen ROIs. (*G* and *H*) Linear relations between the value of C_1, calculated from fitting the linear R_2^* model, and $\Delta\chi$, calculated from the GL model for both white (*G*) and gray (*H*) matter. C_1 and $\Delta\chi$ are related through Eq. **3**. The OD was used as a surrogate for the volume fraction (ζ) of perturbers in these plots.

Correlative Histology of MRI and Myelin Density in Rat Brain Major White Matter Regions. In Fig. 5, the effect of myelin density on C_0 and C_1 was examined. The specific ROIs used for this analysis are given by the black boxes in Fig. 5 *A* and *B*. They include dense white matter regions of the corpus callosum, external capsule, and internal capsule. C_0 and C_1 showed strong positive correlations with myelin OD (Fig. 5 *C* and *E*). C_0 was correlated with myelin OD according to the relation $C_0 = 64.96 \cdot \mathrm{OD} + 37.84$, with $R = 0.905$ and $P < 0.001$ (Fig. 5*C*). C_1 was correlated with myelin OD according to the relation $C_1 = 1.62 \cdot \mathrm{OD} + 0.94$, with $R = 0.456$ and $P < 0.001$ (Fig. 5*E*).

C_0 and C_1 were also computed in six ROIs lining the cortex (green boxes in Fig. 5 *A* and *B*). C_0 and C_1 both demonstrated strong positive correlations with myelin OD in these regions (Fig. 5 *D* and *F*). This supports our hypothesis that an orientation-dependent R_2^* exists in the cortex and the source of this dependence is associated with cortical fibers.

It is noteworthy that R_2 (C_0) and R_2' (C_1) are affected in different ways by changes in myelin density. R_2 is governed by spin–spin interactions between neighboring hydrogen atoms, whereas R_2' is mediated by mesoscopic magnetic field gradients both inside and between voxels. The linear relations derived from the plots in Fig. 5 can be used to independently estimate myelin concentration given either R_2 or R_2'. As well, they support the concept that myelin density and axonal geometry are two major factors governing R_2^* changes observed with changes in fiber orientation.

According to Eq. **3**, the constant C_1, derived from fitting the linear model to the R_2^* orientation data, is a linear function of $\Delta\chi$. To test the validity of this model in both white and cortical gray matter, a value of $\Delta\chi$ was calculated in the black and green ROIs shown in Fig. 5 *A* and *B*, using the GL model. The parameters C_1 and OD were then calculated in these ROIs. The OD value calculated in the ROIs was used as a measure of the volume fraction (ζ). Fig. 5 *G* and *H* illustrate the resulting linear relationships between C_1 and $\Delta\chi$. In white matter a significant linear correlation was observed, verifying that OD can serve as a surrogate marker for perturber volume fraction. However, in cortical gray matter the correlation was not significant, likely due to the poorer fitting of the GL model on a voxel-by-voxel basis in gray matter (as opposed to the case of a single mean value from an ROI shown in Fig. 2*G*). Our paper demonstrates the use of OD as a surrogate marker for volume fraction in white matter microstructure analysis, as well as demonstrates the relationship between R_2^* and $\Delta\chi$ based on the isotropic perturber model. These results suggest that, for white matter, the combined use of R_2^*, $\Delta\chi$, and OD derived from histochemical staining can enhance knowledge of underlying tissue composition.

Conclusion

This study demonstrates a significant orientation dependence of R_2^* in both white and cortical gray matter that is a sinusoidal function of tissue orientation and a linear function of perturber volume fraction. The fitting coefficients, C_0 and C_1, calculated using the R_2^* cylindrical field perturber model, are linearly related to myelin density. For white matter, the isotropic perturber fraction, C_1, is a linear function of the white matter susceptibility difference ($\Delta\chi$) relative to gray matter. This finding supports the premise that a major underlying source of the orientation dependence of R_2^* is the axonal geometry-derived susceptibility shift.

A comparative analysis of the orientation dependencies of R_2^* and f_L in matched tissue locations throughout the rat brains allowed calculation of scaling relations which quantify R_2' given f_L. Using these relations, the orientation-dependent, reversible component of the transverse relaxation rate ($R_2' = \text{constant} \cdot f_L$) was found to be ∼5.60 times larger in white matter compared with gray matter. Measuring such differences in R_2' in different brain tissues is a potential method for probing tissue microstructure, given that R_2' is a function of the geometry-derived, frequency dispersion within a voxel. Equally relevant, the identification of the OD of myelin staining as a realistic surrogate for volume fraction in white and cortical gray matter may complement future studies relating biophysical models of the MRI signal to true underlying tissue composition.

Materials and Methods

Measuring the Orientation Dependence of R_2^* and f_L. The orientation dependence of R_2^* and f_L was experimentally measured in both hemispheres of the rat brain, in white matter fiber tracts and gray matter ($n = 3$ brains, 2 hemispheres, 18 orientations). Each rat brain was scanned with the medial fissure of the brain oriented at 18 different sampling angles relative to the main field of the magnet. Specifically, each brain was rotated to (*i*) 8 unique angles of $n \times 45°$ ($n = 1\ldots8$) around the *y* axis shown in Fig. 1*C*, as well as (*ii*) 10 additional angles chosen to produce an even sampling of the unit sphere. Reproducible rotations were achieved by using the sample holder shown in Fig. 1.

To improve SNR, five contiguous, 100 μm slices in each R_2^* and f_L map were averaged. An average R_2^* and f_L was measured in each ROI specified in Fig. 2*A* (white matter) and Fig. 2 *E* and *I* (gray matter). The orientation of cortical fibers in each gray matter ROI was determined by referencing to a penetrating cortical vein adjacent to, but not included in, the ROI. These veins conveniently define the normal to the cortical surface.

Data from multiple ROIs in each sample are displayed together in Fig. 2 *B–L*. The minimum point of each sinusoidal, orientation-dependence curve from each ROI was phase shifted so that the vector that defined the initial orientation was effectively aligned with the B_0 field. Once the sinusoidal curves were aligned, R_2^* and f_L data for each ROI was averaged for the three animals.

Preparation of Rat Brain Tissue Samples. Three adult, male Sprague–Dawley rats ($n = 3$; 250–300 g) were purchased from Charles River Laboratories. Rat brains were excised and fixed in 4% (vol/vol) formalin solution for 2 wk before imaging. All animal protocols were undertaken in accordance with Animal Care Guidelines, with approval from the Animal Use Subcommittee of University of Western Ontario.

For imaging, the brains were placed inside a 2.5-cm-diameter plastic sphere filled with a magnetic resonance (MR)-invisible, fluorinated solution (Lubrication Technology, Inc.). A custom-machined, spherical sample holder allowed accurate rotation of the brain to image the sample at different angles relative to the field (Fig. 1 *A–C*), while the fluorinated solution minimized the formation of susceptibility-based edge effects in and around the brain.

MRI Protocol. Imaging was performed on a 9.4 T, 31-cm horizontal-bore animal MRI scanner (Agilent Technologies). An in-house–designed B_0 field mapping sequence, robust automated shimming technique using arbitrary acquisition parameters (RASTAMAP) (26), was used to perform automated higher-order shimming before imaging. The rf coil used for all data collection was a 4-cm-diameter millipede coil (Agilent Technologies).

A 3D multiecho gradient-echo acquisition with an imaging field of view of $25.6 \times 25.6 \times 25.6$ mm^3 and an isotropic resolution of 100 μm was used for imaging all brain orientations. The scan parameters were repetition time (TR) = 50 ms, first echo time (TE$_1$) = 3.84 ms, echo spacing = 5.56 ms, and six echoes.

MR Image Postprocessing and Data Analysis. From the multiecho gradient-echo magnitude data, monoexponential R_2^* maps were generated using a Levenberg–Marquardt-weighted least-squares–fitting routine. The variance in the magnitude images was used as a weighting term in the least-squares fitting.

To correct for the influence of B_0 field inhomogeneity, the voxel spread function (VSF) approach was used as described in ref. 27. The VSF method accounts for the combined effects of both through- and in-plane field inhomogeneities, as well as signal leakage from neighboring voxels.

For registration of the data acquired with different brain orientations, the magnitude image corresponding to the second echo at each brain orientation was coregistered to the volume acquired with the medial fissure of the brain aligned at 0° relative to the B_0 field. This was performed using the Oxford Centre for Functional MRI of the Brain's Linear Image Registration Tool (28).

For phase processing, raw phase images were unwrapped in 3D using a region-growing algorithm (29). A Fourier filtering process was then applied to remove background fields. First, a 3D, Gaussian, low-pass filter was applied to the Fourier transform of the unwrapped phase data (30). The Gaussian filter had the following functional form:

$$G(k_x,k_y,k_z) = e^{-\left(k_x{}^2+k_y{}^2+k_z{}^2\right)/2\sigma^2} \quad [7]$$

The value of σ for the convolution kernel was set to 0.007 m^{-1}. This value was chosen to sufficiently remove background field contributions, while still preserving local frequency contrast between gray and white matter. A 3D inverse Fourier transform was then applied to the result of the Fourier domain multiplication to generate low pass-filtered, spatial domain data. Subtraction of this low pass-filtered data from the original, unwrapped phase data produced a high pass filtered phase image.

After background filtering, the phase maps were fit using a weighted linear regression to yield the off-resonance frequency at each voxel, i.e., f_L (31). The linear regression was weighted by the phase noise variances.

Histological Staining. For histological staining, brains were prepared for sectioning using a Leica RM2255 Microtome (Cryostat Microsystems) in accordance with previously published methods (32). Sections were cut at a thickness of 5 μm and deparaffinized before staining by heating at 50 °C. Every second slice was then stained with ScR for myelin detection (32). The remaining slices were stained for iron using DAB-enhanced Perls stain (23).

The microscopy slides were digitized using a Zeiss Axio Optical Imager (Carl Zeiss AG) at 40× magnification. The digital images were then coregistered to the R_2^* maps using the FSL FLIRT registration tool (28). Subsequently, a value for optical density, OD = $\log_{10}(I/I_o)$, was computed at each pixel, where I represents the image intensity for light passing through tissue and I_o represents the image intensity for light passing through a region of the slide where only the background level of staining was observed.

ACKNOWLEDGMENTS. The authors were supported by the Ontario Queen Elizabeth II Graduate Scholarships in Science and Technology fund (D.A.R.), the Canadian Institutes of Health Research (R.S.M.), and the Canada Research Chairs Program (R.S.M.).

1. Bouras C, et al. (1997) A laser microprobe mass analysis of brain aluminum and iron in dementia pugilistica: Comparison with Alzheimer's disease. *Eur Neurol* 38(1):53–58.
2. Chen JC, et al. (1993) MR of human postmortem brain tissue: Correlative study between T2 and assays of iron and ferritin in Parkinson and Huntington disease. *AJNR Am J Neuroradiol* 14(2):275–281.
3. LeVine SM, Wulser MJ, Lynch SG (1998) Iron quantification in cerebrospinal fluid. *Anal Biochem* 265(1):74–78.
4. Sivanandam TM, Thakur MK (2012) Traumatic brain injury: A risk factor for Alzheimer's disease. *Neurosci Biobehav Rev* 36(5):1376–1381.
5. Liu C (2010) Susceptibility tensor imaging. *Magn Reson Med* 63(6):1471–1477.
6. Li W, Wu B, Avram AV, Liu C (2012) Magnetic susceptibility anisotropy of human brain in vivo and its molecular underpinnings. *Neuroimage* 59(3):2088–2097.
7. Schweser F, Sommer K, Deistung A, Reichenbach JR (2012) Quantitative susceptibility mapping for investigating subtle susceptibility variations in the human brain. *Neuroimage* 62(3):2083–2100.
8. Li TQ, et al. (2006) Extensive heterogeneity in white matter intensity in high-resolution T2*-weighted MRI of the human brain at 7.0 T. *Neuroimage* 32(3):1032–1040.
9. Lee J, Hirano Y, Fukunaga M, Silva AC, Duyn JH (2010) On the contribution of deoxy-hemoglobin to MRI gray-white matter phase contrast at high field. *Neuroimage* 49(1): 193–198.
10. Bender B, Klose U (2010) The in vivo influence of white matter fiber orientation towards B(0) on T2* in the human brain. *NMR Biomed* 23(9):1071–1076.
11. Denk C, Hernandez Torres E, MacKay A, Rauscher A (2011) The influence of white matter fibre orientation on MR signal phase and decay. *NMR Biomed* 24(3):246–252.
12. Lee J, et al. (2011) T2*-based fiber orientation mapping. *Neuroimage* 57(1):225–234.
13. He X, Yablonskiy DA (2009) Biophysical mechanisms of phase contrast in gradient echo MRI. *Proc Natl Acad Sci USA* 106(32):13558–13563.
14. de Rochefort L, et al. (2010) Quantitative susceptibility map reconstruction from MR phase data using bayesian regularization: Validation and application to brain imaging. *Magn Reson Med* 63(1):194–206.
15. Yablonskiy DA, Haacke EM (1994) Theory of NMR signal behavior in magnetically inhomogeneous tissues: The static dephasing regime. *Magn Reson Med* 32(6): 749–763.
16. Cohen-Adad J, et al. (2012) T_2* mapping and B_0 orientation-dependence at 7 T reveal cyto- and myeloarchitecture organization of the human cortex. *Neuroimage* 60(2): 1006–1014.
17. Li L, Leigh JS (2004) Quantifying arbitrary magnetic susceptibility distributions with MR. *Magn Reson Med* 51(5):1077–1082.
18. de Rochefort L, Brown R, Prince MR, Wang Y (2008) Quantitative MR susceptibility mapping using piece-wise constant regularized inversion of the magnetic field. *Magn Reson Med* 60(4):1003–1009.
19. Liu C, Li W, Johnson GA, Wu B (2011) High-field (9.4 T) MRI of brain dysmyelination by quantitative mapping of magnetic susceptibility. *Neuroimage* 56(3):930–938.
20. Shepherd TM, Thelwall PE, Stanisz GJ, Blackband SJ (2009) Aldehyde fixative solutions alter the water relaxation and diffusion properties of nervous tissue. *Magn Reson Med* 62(1):26–34.
21. Ogawa S, Lee TM, Kay AR, Tank DW (1990) Brain magnetic resonance imaging with contrast dependent on blood oxygenation. *Proc Natl Acad Sci USA* 87(24):9868–9872.
22. Luo J, He X, Yablonskiy DA (2013) Magnetic susceptibility induced white matter MR signal frequency shifts-experimental comparison between Lorentzian sphere and generalized Lorentzian approaches. *Magn Reson Med*, 10.1002/mrm.24762.
23. Fukunaga M, et al. (2010) Layer-specific variation of iron content in cerebral cortex as a source of MRI contrast. *Proc Natl Acad Sci USA* 107(8):3834–3839.
24. Yao B, et al. (2009) Susceptibility contrast in high field MRI of human brain as a function of tissue iron content. *Neuroimage* 44(4):1259–1266.
25. Deistung A, et al. (2013) Toward in vivo histology: A comparison of quantitative susceptibility mapping (QSM) with magnitude-, phase-, and R2*-imaging at ultra-high magnetic field strength. *Neuroimage* 65:299–314.
26. Klassen LM, Menon RS (2004) Robust automated shimming technique using arbitrary mapping acquisition parameters (RASTAMAP). *Magn Reson Med* 51(5):881–887.
27. Yablonskiy DA, Sukstanskii AL, Luo J, Wang X (2012) Voxel spread function method for correction of magnetic field inhomogeneity effects in quantitative gradient-echo-based MRI. *Magn Reson Med* 70(5):1283–1292.
28. Jenkinson M, Smith S (2001) A global optimisation method for robust affine registration of brain images. *Med Image Anal* 5(2):143–156.
29. Abdul-Rahman HS, et al. (2007) Fast and robust three-dimensional best path phase unwrapping algorithm. *Appl Opt* 46(26):6623–6635.
30. Rauscher A, Barth M, Reichenbach JR, Stollberger R, Moser E (2003) Automated unwrapping of MR phase images applied to BOLD MR-venography at 3 Tesla. *J Magn Reson Imaging* 18(2):175–180.
31. Kressler B, et al. (2010) Nonlinear regularization for per voxel estimation of magnetic susceptibility distributions from MRI field maps. *IEEE Trans Med Imaging* 29(2): 273–281.
32. Roscoe WA, Welsh ME, Carter DE, Karlik SJ (2009) VEGF and angiogenesis in acute and chronic MOG((35-55)) peptide induced EAE. *J Neuroimmunol* 209(1-2):6–15.